Anomalous Refractive Index Modulation and Giant Birefringence in 2D Ferrielectric $CuInP_2S_6$

El Mrabet Haje, Houssam; van der Kolk, Roald J.H.; Kyrk, Trent M.; Grytsiuk, Sergii; Rösner, Malte; Ali, Mazhar N.

DOI
10.1002/adom.202502291

Publication date
2025

Document Version
Final published version

Published in
Advanced Optical Materials

RESEARCH ARTICLE

ADVANCED OPTICAL MATERIALS
www.advopticalmat.de

Anomalous Refractive Index Modulation and Giant Birefringence in 2D Ferrielectric $CuInP_2S_6$

Houssam El Mrabet Haje, Roald J.H. van der Kolk, Trent M. Kyrk, Sergii Grytsiuk, Malte Rösner, and Mazhar N. Ali**

2D ferroelectric (FE) materials have opened new opportunities in non-volatile memories, computation and non-linear optics due to their robust polarization in the ultra-thin limit and inherent flexibility in device integration. Recently, interest has grown in the use of 2D FEs in electro-optics, demanding the exploration of their electronic and optical properties. In this work, the discovery of an unprecedented anomalous thickness-dependent change in refractive index, as large as $\delta n \sim 23.2\%$, is reported in the 2D ferrielectric $CuInP_2S_6$, far above the ultra-thin limit, and at room temperature. It is also shown that the anomalous behavior in $CuInP_2S_6$ may be generalizable to other ferroelectric materials such as $LiNbO_3$. Furthermore, $CuInP_2S_6$ exhibits a giant birefringence in the blue-ultraviolet regime, with a maximum $|n_{OOP} - n_{IP}| \sim 1.24$ at $t \sim 22$ nm and $\lambda = 339.5$ nm, which is, to the best of our knowledge, the largest of any known material in this wavelength regime. Changes in the optical constants of $CuInP_2S_6$ are related to changes in the Cu(I) FE polarization contribution, inducing changes in its ionic mobility, and opening the door to electronic control of its optical response for use in photonics and electro-optics.

1. Introduction

As a result of the increasing need for highly efficient, tunable, and high-speed electro-optic devices in modern-day telecommunications,[1,2] sensing[3] and quantum technologies,[4] there has been a surge of interest in 2D FEs. They have shown non-linear and tunable optical and electronic properties[5–7] with the potential to surpass contemporary 3D ferroelectric electro-optic platforms like $LiNbO_3$.[2] For instance, materials with large birefringence, particularly within the visible-ultraviolet range, are essential for light polarization manipulation,[8–10] ultraviolet communications,[11] and lithography,[12,13] making them highly desired in the fields of photonics and integrated electro-optics. Typical platforms either suffer from low optical anisotropy,[14–16] high losses[17] or integration and stability concerns.[16–19] 2D FEs, due to their crystalline anisotropy and non-linear behaviors, present themselves as attractive new platforms in these fields.

Amongst the 2D FEs that have garnered significant attention, $CuInP_2S_6$ (CIPS) stands out due to its moderate band gap $E_g \sim 2.8$ eV,[20–22] robust ferrielectricity at room temperature ($T_c \sim 315$ K) even to the ultra-thin limit,[23–26] and remarkable ionic conductivity.[27,28] This has led to observations of pyroelectricity down to the thin limit,[26] giant negative piezoelectricity,[29] enhanced bulk photovoltaic effect,[30] and more.[31–34] Hence, CIPS is actively being investigated for its potential in varying fields, including nanoelectronics,[35] photonics,[36] electro-optics,[37] and others.[38–41]

The driving force behind the technologically relevant behaviors of CIPS are its Cu(I) cations, which contribute significantly to both its ferrielectricity and ionic conductivity.[23,42–44] The crystal structure of CIPS (**Figure 1a**) is built from planar layers of filled sulfur octahedra, where the central voids are occupied by either P-P dimers, In(III) cations, or Cu(I) cations. At $T > T_c$, the Cu(I) ions are spatially disordered, giving rise to a paraelectric ionic conducting state. At room temperature, CIPS exists in a ferrielectric ionic conductive state due to a second-order Jahn-Teller distortion, where the Cu(I) cations partially occupy three positions: within the sulfur framework at a quasi-trigonal site, at an octahedral site, and within the van der Waals gap in a quasi-tetrahedral site. Consequently, In(III) cations displace in the opposite

H. El Mrabet Haje, T. M. Kyrk, M. N. Ali
Department of Quantum Nanoscience
Faculty of Applied Sciences
Delft University of Technology
Delft 2628 CJ, Netherlands
E-mail: H.elMrabetHaje@tudelft.nl; M.N.Ali@tudelft.nl

H. El Mrabet Haje, R. J. van der Kolk, T. M. Kyrk, M. N. Ali
Kavli Institute of Nanoscience
Delft University of Technology
Delft 2628 CJ, Netherlands

R. J. van der Kolk
Department of Imaging Physics
Faculty of Applied Sciences
Delft University of Technology
Delft 2628 CJ, Netherlands

S. Grytsiuk, M. Rösner
Institute for Molecules and Materials
Radboud University
Nijmegen 6525 AJ, Netherlands

M. Rösner
Faculty of Physics
Bielefeld University
33501 Bielefeld, Germany

DOI: 10.1002/adom.202502291

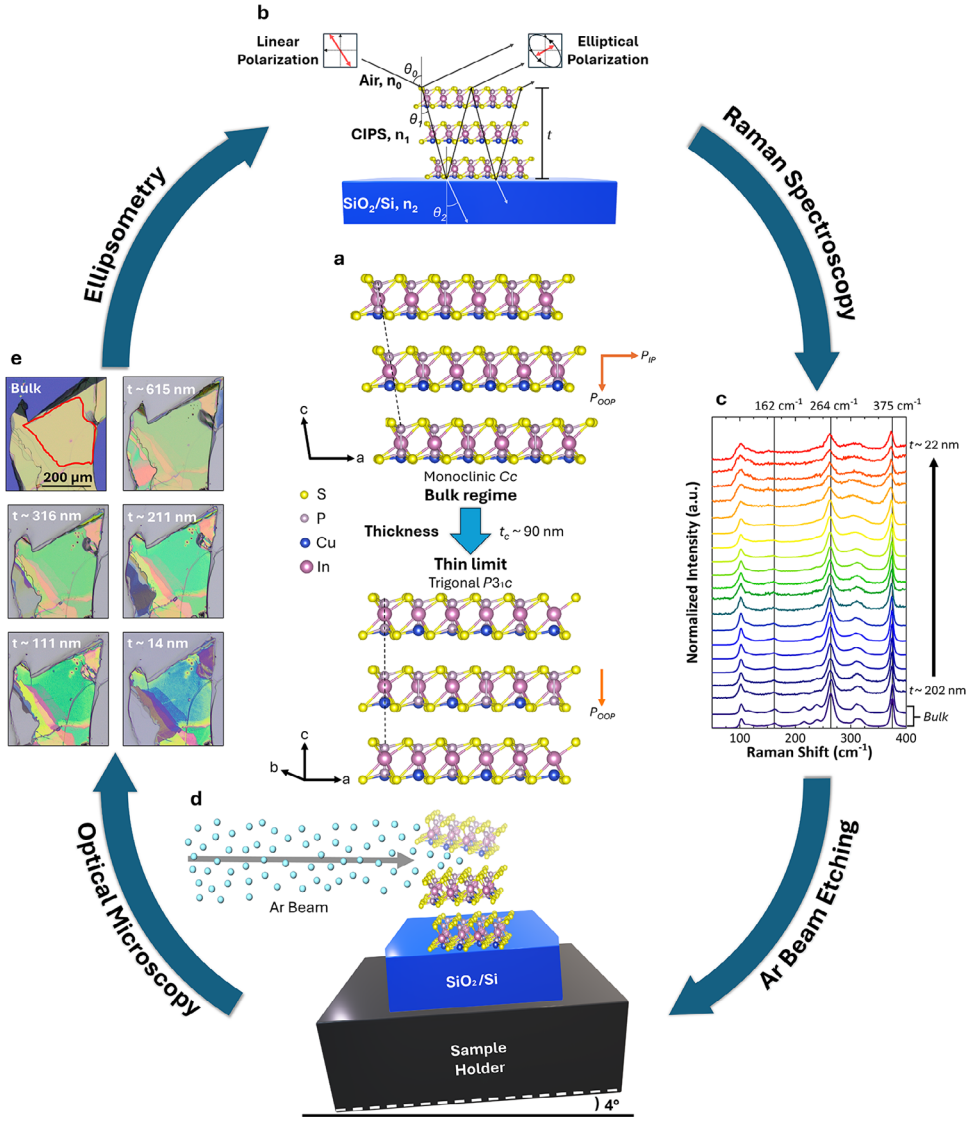

Figure 1. Experimental methodology cycle. a) Side-view of the thickness-induced structural transition in CIPS from monoclinic *Cc*[49] to trigonal $P3_1c$.[45] Here, t is the thickness of the CIPS flake and t_c is the critical thickness at which the phase transformation occurs. The orange arrows indicate the in-plane ($\vec{P}_{IP}$) and out-of-plane ($\vec{P}_{OOP}$) polarizations. For $t > t_c$, the total polarization is $\vec{P}_T = \vec{P}_{IP} + \vec{P}_{OOP}$. For $t < t_c$, $\vec{P}_T = \vec{P}_{OOP}$. b) Schematic of the spectroscopic ellipsometry measurements performed on CIPS, where θ_0 is the incident angle, θ_1 is the refracted angle of light in CIPS, and θ_2 is the refracted angle of light in the substrate. The refractive index of light in air, CIPS, and SiO_2 is denoted as n_0, n_1, and n_2, respectively. c) Collection of all the normalized Raman spectra of CIPS from bulk to $t \sim 22$ nm. Black lines indicate peak positions of relevant vibrational modes. d) Side-view schematic of the low-angle argon beam etching procedure used to reduce the thickness of the CIPS flake. e) Optical microscope images of the CIPS flake at different thicknesses, with the area studied by ellipsometry and Raman spectroscopy outlined in red.

direction with respect to Cu(I) cations, generating a spontaneous and non-compensated out-of-plane (OOP) polarization.[23,42]

The Cu(I) cations in CIPS also displace within the plane, generating a thickness-dependent in-plane (IP) polarization.[45,46] Below critical thickness t_c (reported to be at $t \sim 90$ nm[45]), a structural phase transition occurs, where the molecular layers of CIPS slide along the $\vec{a}$ direction, changing the crystal symmetry from monoclinic *Cc* to trigonal $P3_1c$ (Figure 1a), and causing the IP polarization to disappear while preserving the OOP polarization.[45,47] Other thickness-dependent behaviors in CIPS have been observed, including an increase of the electrocaloric effect at $t \sim 169$ nm,[34] an abrupt decrease of the piezoelectric coefficient d_{33} at $t < 40$ nm,[35] and an enhancement of the bulk photovoltaic effect at $t < 80$ nm,[30] among others.[32,33,38,47,48] However, as yet, the optical properties of CIPS and their anisotropies have not been thoroughly investigated as a function of thickness. Of particular interest are its refractive index n, extinction coefficient κ, and dielectric function $\hat{\varepsilon} = \varepsilon_1 + i\varepsilon_2$, as well as its birefringence Δn and dichroism $\Delta\kappa$.

Here we investigate the thickness and wavelength dependencies of the in-plane and out-of-plane optical constants of CIPS, as well as its optical anisotropy, from the bulk to the thin limit

using Variable Angle Spectroscopic Ellipsometry (VASE). We also characterize the vibrational modes of CIPS using Raman spectroscopy. We observe an anomalous change in optical constants as a function of thickness as large as $\delta n \sim 23.2\%$ and within $t \in [22, 170)$ nm, which we attribute to changes in the polarization of CIPS stemming from the Cu(I) component and, potentially, its ion mobility. Moreover, we also show that CIPS exhibits giant intrinsic birefringence $|\Delta n| = |n_{OOP} - n_{IP}|$ for the entire range of wavelengths studied $\lambda \in [210.6, 1688.3]$ nm, with a maximum $|\Delta n| \sim 1.24$ at $t \sim 22$ nm and $\lambda = 339.5$ nm, which is, to the best of our knowledge, the largest of any known material in the blue-ultraviolet regime. Both discoveries, the anomalous change of refractive index with thickness and the giant birefringence in CIPS, reveal thickness as a new tuning parameter and lay the groundwork for 2D ferroelectrics to be used as non-linear and tunable platforms for electro-optical control, even far from the ultra-thin limit and in a broad spectral range.

2. Results

To investigate the thickness and wavelength-dependent optical properties of CIPS, a bulk flake was exfoliated onto a SiO_2/Si substrate (see Section 5 for details). The thickness and optical constants were extracted for wavelengths $\lambda \in [210.6, 1688.3]$ nm using VASE, as illustrated in Figures 1b and S1a. Subsequently, Raman spectroscopy was performed to measure the vibrational modes of CIPS (Figure 1c), followed by a thinning of the CIPS flake by approximately 10 nm using low-angle argon beam etching to minimize damage to the crystal structure of the flake (Figures 1d and S1b). With this new thickness (Figure 1e), the flake was again measured using VASE and Raman and the cycle was repeated until reaching a thickness of $t \sim 14$ nm. Following this sequence, we were able to study the effects of thickness and wavelength on the optical constants and the vibrational spectrum of CIPS.

Additional ferroelectric, surface, and chemical characterization of CIPS was performed to confirm its ferroelectricity and to validate the appropriateness of the novel etching technique we used, by means of piezoresponse force microscopy (PFM), atomic force microscopy (AFM), and energy dispersive X-ray spectroscopy (EDS), respectively. In Figures S2b,c we show the PFM amplitude and the PFM phase of a CIPS flake, proving the existence of FE domains with opposite direction and similar amplitude, in contrast to the results for an hBN flake used as a non-ferroelectric control experiment. Moreover, the presence in Figure S2d of both a hysteretic loop for the PFM phase and the butterfly-like shape loop in the PFM amplitude of CIPS, absent in hBN, further confirms its ferroelectric nature. On the other hand, Figure S1c presents

the AFM topography of the CIPS plateau used in this work after hours of etching, where surface cracks denoting damage to the plateau are absent. Similar behavior can be observed in Figure S1d for a different CIPS flake. To further confirm the structural integrity of CIPS after etching, Figure S3 shows the chemical composition characterization of a CIPS flake, as-exfoliated, after 15 min of etching, and after 60 min of etching. Considering the reliability of EDS to measure thin flakes, no major changes in the stoichiometry of CIPS can be observed.

2.1. Effect of thickness on optical constants

Figures 2 and S4 present the IP and OOP refractive indices and extinction coefficients of CIPS at different thicknesses as a function of wavelength. The IP refractive index of CIPS (Figure 2a) peaks at $\lambda \sim 350$ nm. As thickness decreases, the maximum refractive index shifts to longer wavelengths but decreases in magnitude, from $n \sim 3.6$ at $t \sim 615$ nm and $\lambda = 345.8$ nm, to $n \sim 3.5$ at $t \sim 22$ nm and $\lambda = 353.8$ nm. However, there is a crossing point at $\lambda \sim 1320$ nm (Figure S4a), where for longer wavelengths the refractive index increases with decreasing thickness. Similarly, the maximum IP extinction coefficient (Figure 2b) shifts to longer wavelengths as thickness decreases, but displays a crossing point at $\lambda \sim 274$ nm, where the thickness dependence trend inverts. At $t \sim 615$ nm and $\lambda \sim 456$ nm, a kink is visible that continuously shifts to $\lambda \sim 441$ nm at $t \sim 22$ nm as thickness decreases, which aligns well with the band gap previously reported for CIPS of $E_g \sim 2.8$ eV ($\lambda \sim 443$ nm).[20–22]

In contrast, the OOP refractive index (Figure 2c) and extinction coefficient (Figure 2d) exhibit completely different dependencies. For the OOP refractive index, the local maximum of $n \sim 2.8$ at $t \sim 615$ nm and $\lambda = 280.5$ nm continuously decreases in magnitude as the thickness decreases. At $t \in [60, 83)$ nm the feature becomes undetectable, and by $t \sim 22$ nm it has merged with the minimum at shorter wavelengths already present in the bulk, with $n \sim 2.1$ at $\lambda = 282.1$ nm. Hence, around $\lambda \sim 280$ nm, wavelength at which CIPS has been reported to be a high-performance ultraviolet photodetector,[50] we obtain the largest change in refractive index with thickness. Simultaneously, a second peak emerges when $t \in (161, 170]$ nm, becoming a new local maximum with a refractive index of $n \sim 2.4$ at $t \sim 22$ nm and $\lambda = 383.9$ nm. Regarding the OOP extinction coefficient, there is a maximum in the extinction coefficient, with $\kappa \sim 0.50$ at $t \sim 615$ nm and $\lambda = 269.5$ nm, that decreases with thickness, flattening at $t \in [60, 83)$ nm. Concomitantly, a second peak emerges at $t \in (161, 170]$ nm, with a maximum in the OOP extinction coefficient of $\kappa \sim 0.38$ at $t \sim 22$ nm and $\lambda = 352.2$ nm. The change in maxima in the OOP extinction coefficient results in a crossing point similar to that observed in the IP, but in this case at $\lambda = 295.0$ nm.

When comparing the IP and OOP optical constants, CIPS unequivocally exhibits giant birefringence $|\Delta n| = |n_{OOP} - n_{IP}| > 0.3$ and dichroism $|\Delta \kappa| = |\kappa_{OOP} - \kappa_{IP}| > 0.3$, both in the bulk regime, as previously demonstrated,[51–53] and most strongly in the few-nanometer regime (Figure S5). The dichroism is locally maximized at $t \sim 22$ nm and $\lambda = 253.5$ nm, with $|\Delta \kappa| \sim 1.55$, while the birefringence is maximized at $t \sim 22$ nm and $\lambda = 339.5$ nm, with $|\Delta n| \sim 1.24$. Δn changes sign as we decrease the wavelength from negative to positive at $\lambda \sim 244$ nm, and remains giant for all measured thicknesses.

Figures 3 and S7 show the thickness-dependent IP and OOP refractive index and extinction coefficients of CIPS for $t \in (14, 600]$ nm at three significant wavelengths: $\lambda = 280.0$ nm (the wavelength at which the change of refractive index with thickness in CIPS is the largest, see Figure 2c), $\lambda = 632.8$ nm (commonly used wavelength in optics), and $\lambda = 1550.0$ nm (commonly used wavelength in telecommunications). For $t \geqslant 170$ nm, the optical constants of CIPS remain constant with thickness as expected (albeit with an offset occurring at $t \sim 390$ nm). Within the thickness range $t \in [22, 170)$ nm, an anomalous thickness dependence is

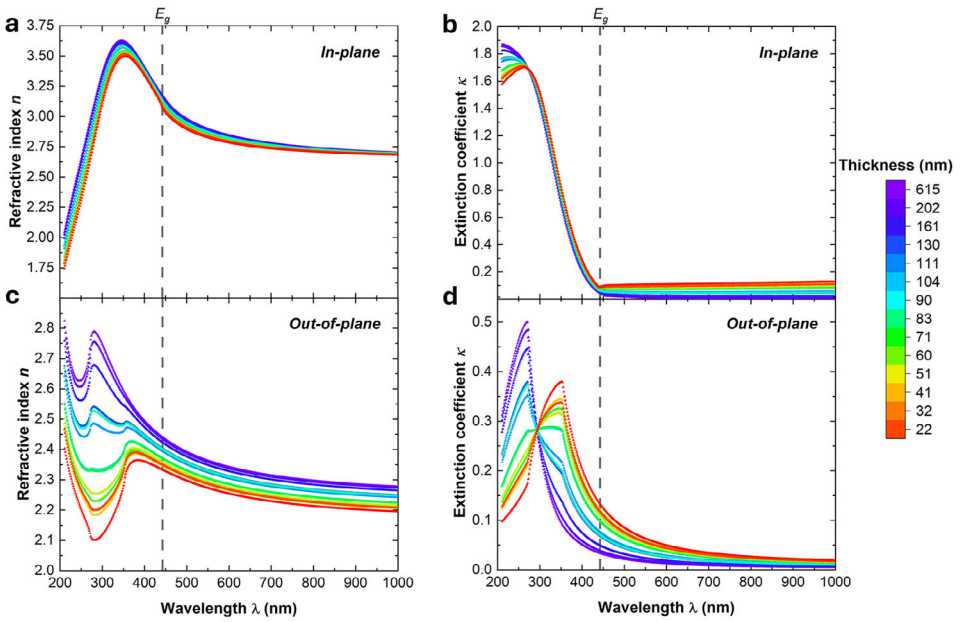

Figure 2. Optical constants wavelength dependence of CIPS. The wavelength-dependent a) in-plane and c) out-of-plane refractive indices and b) in-plane and d) out-of-plane extinction coefficients of CIPS at different thicknesses. The dashed lines correspond to the reported band gap value of CIPS $E_g \sim 2.8$ eV ($\lambda \sim 443$ nm).[20–22]

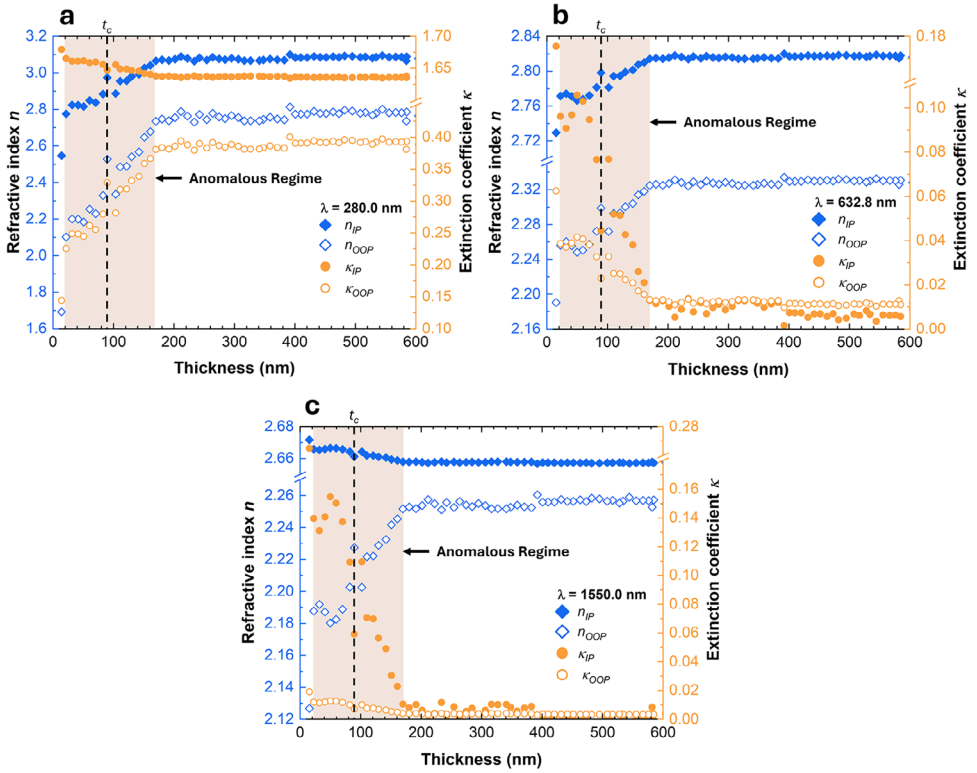

Figure 3. Optical constants thickness dependence of CIPS. In-plane and out-of-plane thickness dependence refractive index and extinction coefficient of CIPS at three significant wavelengths: a) $\lambda = 280.0$ nm, b) $\lambda = 632.8$ nm, and c) $\lambda = 1550.0$ nm. The orange shaded area corresponds to the anomalous thickness regime $t \in [22, 170)$ nm. The dashed line at $t_c \sim 90$ nm corresponds to the thickness of CIPS below which the IP polarizations disappears according to ref. [45].

observed for both the IP and OOP optical constants, together with a large change in refractive index with thickness. Lastly, below $t \sim$ 22 nm we encounter the thin limit, where finite size effects play a pivotal role in the material's properties and immense changes in the optical constants of CIPS are observed, a phenomenon also reported for various 2D and 3D materials.[54–60] Considering that the electro-optic coefficient of bulk CIPS[61] is comparable to typical 3D materials like $LiNbO_3$,[62,63] CIPS flakes within the anomalous thickness regime are a promising platform for large electro-optic modulation.

For the range of wavelengths studied and within the anomalous regime, CIPS exhibits a thickness-dependent change in the OOP refractive as large as 23.2% at λ = 280.0 nm (Table S1). However, in the thickness range $t \in$ [22, 50] nm, the optical constants of CIPS show a different trend compared to the rest of the anomalous regime. This change in habit could signify either a gradual leveling-off of the thickness-dependent effect or a change in mechanism for the behavior. Another sudden change is also observed for all optical constants, regardless of wavelength or direction, around $t \sim$ 90 nm, coinciding with the critical thickness t_c reported in ref. [45], below which the IP polarization ceases to exist. Considering that the refractive index of a FE is coupled to its polarization,[64,65] the rapid change in optical constants observed at $t \sim$ 90 nm may be explained by the IP polarization loss in CIPS. Nevertheless, the anomalous behavior above and below $t \sim$ 90 nm cannot be explained by this. To attempt to better understand the relationship between the crystal structure of CIPS and its anomalous optical regime, we also carried out thickness-dependent Raman measurements.

2.2. Thickness-dependent Raman spectroscopy

The Raman-active vibrational modes of CIPS were investigated between [100, 400] cm^{-1} using Raman spectroscopy for thicknesses $t \in$ [22, 202] nm. **Figure** 4a shows the normalized Raman spectrum of bulk CIPS, in good agreement with previous reports.[61,66–69] As seen in Figure 1c, the absence of extra peaks as the CIPS flake is thinned from bulk to the few nanometer regime confirms that argon beam etching does not cause significant damage to the crystal structure of CIPS.[70] Furthermore, there are no signatures to indicate the formation of $In_{4/3}P_2S_6$ through Cu(I) deficiencies, which would lead to a different Raman fingerprint than observed for CIPS.[69]

Figures 4b-e present the thickness-dependent peak positions of four vibrational modes: Cu^+, S-P-P, S-P-S, and P-P. More peak positions are included in Figure S9. Despite the presence of a few outliers, a clear shift in peak position is observed at $t \in$ [60, 71] nm for the P-P, S-P-S and S-P-P, while the shift for the Cu^+ peak can be found at $t \in$ [71, 83] nm. In both cases, the shift is sharp, distinctive of a first-order phase transition.[70] For the case of the Cu^+ peak (Figure 4b), the shift in peak position with thickness agrees reasonably well with the shift reported in ref. [32].

The shift in position of the P-P, S-P-P and S-P-S vibrational modes at $t \in$ [60, 71] nm might relate to the thickness-induced structural transition of CIPS. In Figures 2c-d, we observed shifts in the trends below $t \sim$ 60 nm, which may have been induced by this transition, potentially in parallel with other phenomena. Furthermore, the shift in position of the Cu^+ peak at $t \in$ [71, 83] nm may relate to changes in Cu(I) occupancy within its possible three positions. In ref. [71] it was shown that the broad peak at T = 300 K evolves into three peaks at T = 78 K. Analogously, we observed that while maintaining room-temperature conditions but decreasing thickness, the Cu^+ peak's width increases (Figure S9a), implying an increase in Cu(I) disorder[70] linked to a change in Cu(I) occupancies, hence a change in Cu(I) polarization. Therefore, from the Raman data we believe that a change in the polarization of CIPS takes place prior to its thickness-induced structural transition, which may explain the anomaly CIPS exhibits in the thickness-dependent optical constants at $t \sim$ 90 nm.

We have corroborated the thickness-induced phase transformation in CIPS, and we have demonstrated that changes in the polarization of CIPS may already occur above its critical thickness $t_c \in$ [60, 71] nm, impacting its optical constants (sudden change in refractive index and extinction coefficient at $t \sim$ 90 nm). In order to determine the origin of the anomalous thickness regime in CIPS, we now proceed to compare the thickness-dependent refractive index of CIPS to commonly used dielectrics and FEs.

2.3. Comparison of thickness-dependent effects

To better understand the uniqueness of the anomalous thickness-dependent optical constants in CIPS, and as control experiments, we performed thickness-dependent VASE studies on two widely used materials, $LiNbO_3$ and SiO_2 (Figure S10). **Figures** 5a and S11 show the ratio between the refractive index at a certain thickness n_t and the refractive index at the maximum thickness value n_{Bulk} for different materials as a function of thickness. The refractive index of dielectric materials (e.g. SiO_2, Ta_2O_5) remains constant as thickness decreases ($n_t/n_{Bulk} \sim 1$) until the few-nanometer limit, where abrupt changes are expected and observed due to finite size effects. However, materials with ferroelectric nature, like 2D ferrielectric CIPS (this work), as well as 3D ferroelectric $LiNbO_3$ (this work) and 3D multiferroic Bi_2FeCrO_6,[59] show modulation of its refractive index as a function of thickness, indicating that the anomalous behavior observed in CIPS may be generalizable to other ferroelectrics, but to a lesser extent. To the best of our knowledge, both the anomalous refractive index thickness dependence of CIPS, and its extension to other ferroelectrics have not been reported prior to this work, presenting a new tuning parameter for control.

Figure 5b shows the intrinsic birefringence $|\Delta n| = |n_{OOP} - n_{IP}|$ of CIPS at $t \sim$ 22 nm as a function of wavelength compared to various contemporary birefringent materials. Notably, the birefringence of CIPS, particularly in the blue-ultraviolet range, outperforms typically used 3D materials (quartz, calcite,[15,72] rutile,[14] and others[73,74]) as well as other low-dimension materials (2D: hBN,[75] transition metal dichalcogenides,[76,77] and others;[78–80] quasi-1D: $BaTiS_3$;[81] and 0D: $[(p\text{-}C_5H_5NO)_2ZnCl_2]$[82]), intrinsically, without the benefit of metasurface engineering.[83]

3. Discussion

To address the origin of the observed anomalous thickness-dependent change in the optical constants of CIPS for $t \in$ [22,

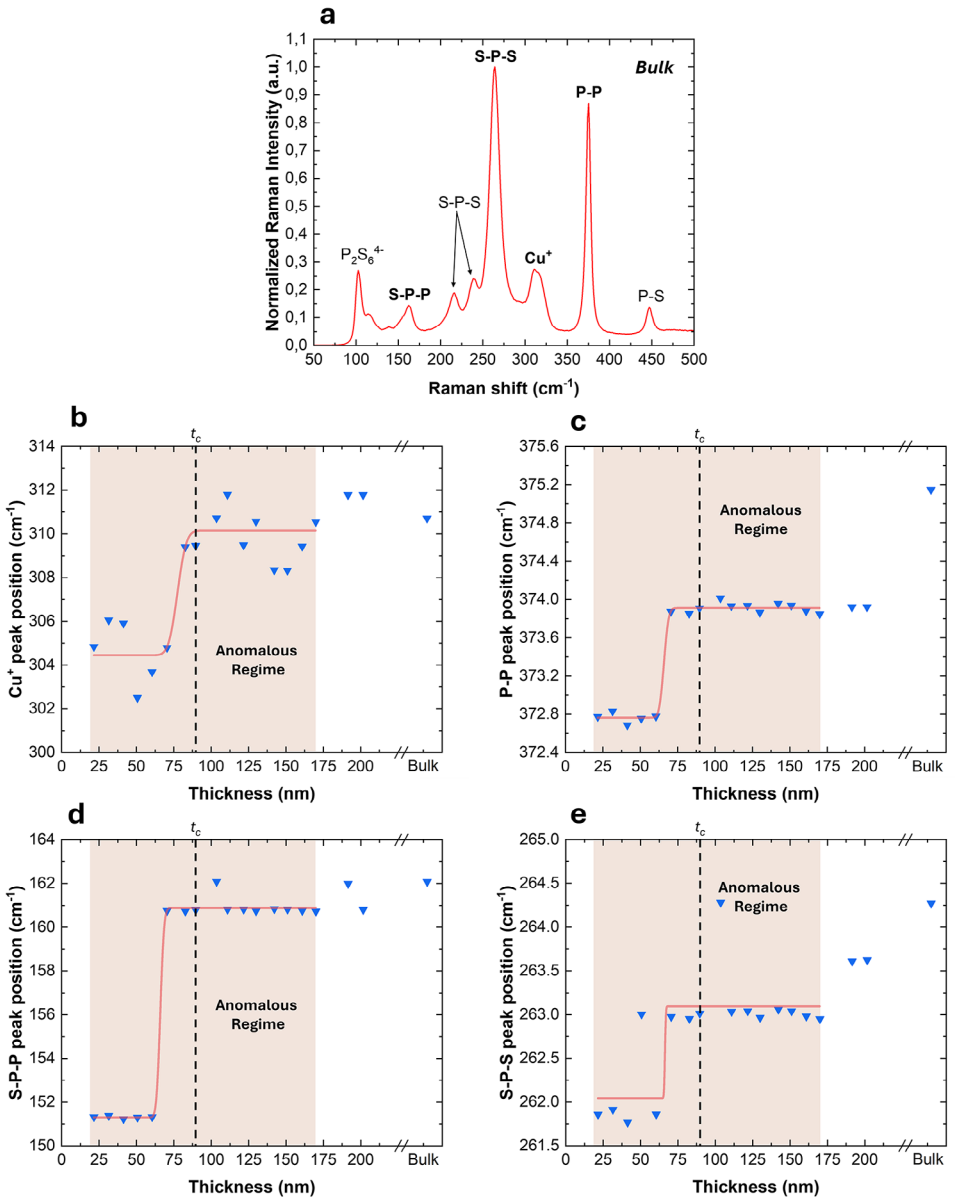

Figure 4. Raman spectrum thickness dependence of CIPS. a) Bulk normalized Raman spectrum of CIPS in the range of Raman shifts $\omega \in [100, 400]$ cm^{-1}, with the vibrational modes of CIPS ascribed to their respective peaks: $\omega \sim 102.5$ cm^{-1}, $\omega \sim 114.5$ $cm^{-1} \rightarrow P_2S_6^{-4}$, $\omega \sim 162$ $cm^{-1} \rightarrow$ S-P-P, $\omega \sim 216$ cm^{-1}, $\omega \sim 238.5$ cm^{-1}, $\omega \sim 264$ $cm^{-1} \rightarrow$ S-P-S, $\omega \sim 311$ $cm^{-1} \rightarrow Cu^{+}$, and $\omega \sim 375$ $cm^{-1} \rightarrow$ P-P. In bold, the Raman shifts (vibrational modes) emphasized in this thickness-dependence study: b) $\omega(t) \sim 311$ $cm^{-1} \rightarrow$ **Cu^{+}**, c) $\omega(t) \sim 375$ $cm^{-1} \rightarrow$ **P-P**, d) $\omega(t) \sim 162$ $cm^{-1} \rightarrow$ **S-P-P**, and e) $\omega(t) \sim 264$ $cm^{-1} \rightarrow$ **S-P-S**. The shaded area corresponds to the anomalous thickness regime of CIPS $t \in [22, 170)$ nm. The dashed line at $t \sim 90$ nm corresponds to the thickness below which the IP polarizations of CIPS disappears according to ref. [45]. The red lines correspond to data fitting using the error function.

170] nm, we briefly discuss five possible extrinsic and intrinsic mechanisms: substrate-induced strain, laser-induced heating, resonance between FE domain size and flake thickness, depolarization, and finally ferro-ionic effects.

Selhorst et al.[67] observed an increase in Raman peak frequencies for $t < 50$ nm CIPS flakes, which they attribute to substrate-induced strain. If the origin of our observed Raman shifts is substrate-induced strain, as the thickness of the flake decreases, the strain suffered by the flake would increase,[84] necessitating a continuous change of the Raman peak frequencies with thickness, similar to what Selhorst et al. observe in the ultra-thin regime. Yet, we do not observe such behavior and given the lack of additional strain sources, substrate-induced effects appear to be insufficient to account for the observed trends, in agreement with the thickness-dependence Raman results reported in ref. [32].

Another possible origin for the observed shifts in the vibrational modes of CIPS could be laser-induced heating during Raman measurements. In the work from Dey,[66] non-negligible shifts in Raman peaks were observed using a laser power of 20 mW. Anticipating this issue, we used a much lower power of 0.5 mW. Additionally, if our irradiation power was too large, we would expect the shift of the different vibrational modes to move

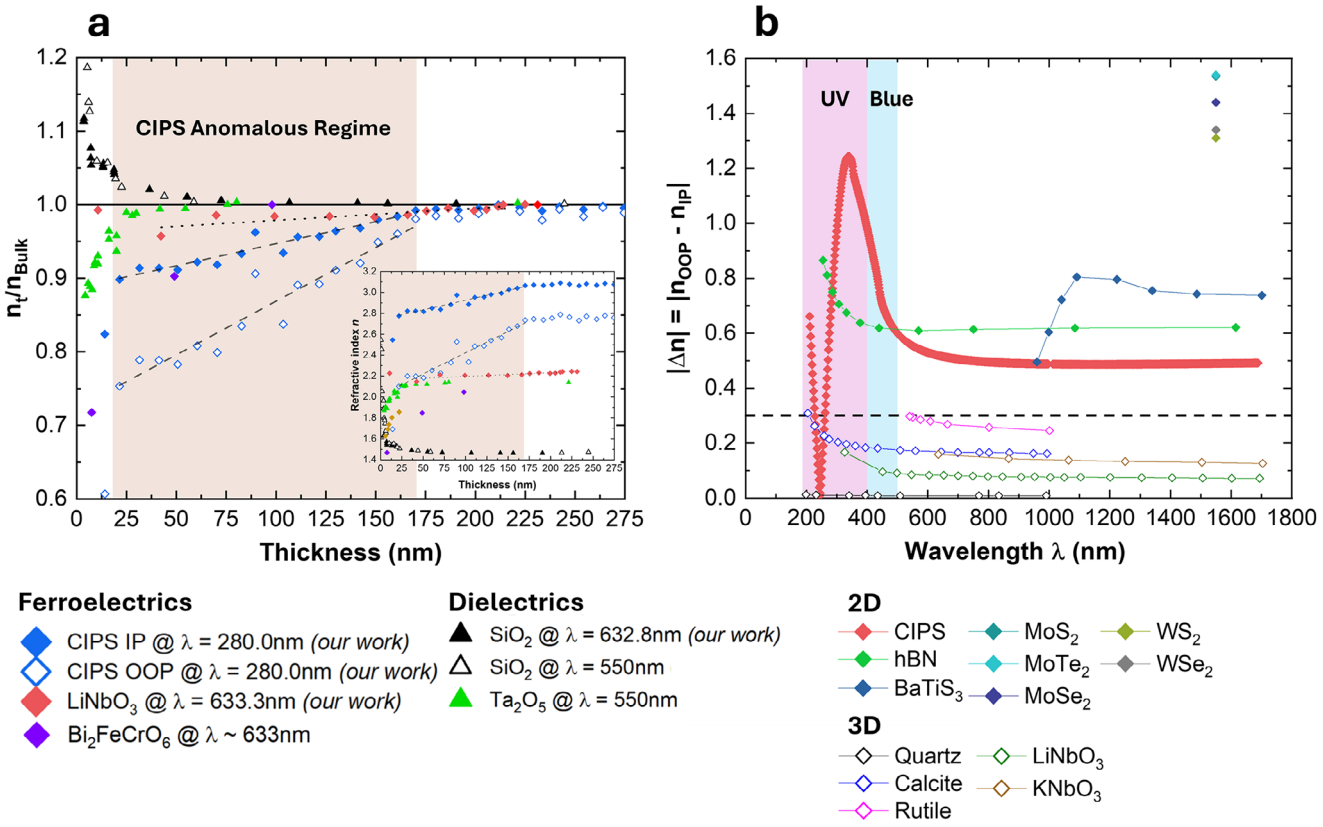

Figure 5. Optical properties for various materials. a) Refractive index thickness dependence comparison between this work's materials (IP and OOP CIPS, $LiNbO_3$ and SiO_2) and other materials in the literature (SiO_2,[56] Ta_2O_5,[58] and Bi_2FeCrO_6[59]). n_t/n_{Bulk} represents the ratio between the refractive index at a certain thickness (n_t) and the refractive index at the maximum thickness (n_{Bulk}). The shaded area corresponds to the anomalous thickness regime of CIPS $t \in [22, 170)$ nm. The dashed and the dotted lines show linear fittings of the CIPS and $LiNbO_3$ data, respectively. The inset shows the raw refractive index thickness dependencies. b) Birefringence $|\Delta n| = |n_{OOP} - n_{IP}|$ comparison between CIPS at $t \sim 22$ nm and other materials in the literature: hBN,[75] $BaTiS_3$,[81] MoS_2,[76] $MoTe_2$, $MoSe_2$, WS_2, WSe_2,[77] quartz, calcite,[15] rutile,[14] $LiNbO_3$,[73] and $KNbO_3$.[74] The dashed line sets the threshold at which materials are defined to have giant birefringence. The violet and blue shaded areas correspond to the UV and blue wavelength ranges, respectively.

to lower frequencies continuously with thickness, rather than the sudden step-like shift observed in Figures 4b-e, making it unlikely for laser heating to account for our observations.

Beyond extrinsic mechanisms and regarding the thickness-dependent optical results of this work, we do not attribute the anomalous regime at $t \in [22, 170)$ nm to arise from FE domain formation of size similar to the thickness of the CIPS flake. In ref. [85] it was shown that the FE domains in CIPS follow a Landau-Lifshitz-Kittel law within the thickness range $t \in (10, 130)$ nm, where $W \sim t^m$, with W being the characteristic size of the FE domains, t the thickness of the flake, and $m = 0.65$, meaning that the FE domains in CIPS would be much smaller than the thickness of the crystal.

Finally, as we think the CIPS flake, we consider the depolarization field as a continuous source of polarization change with thickness,[86,87] which would lead to continuous changes in the optical constants. However, the anomalous optical response observed in this work starts at a thickness $t \sim 170$ nm; atypically high to be related to depolarization effects.[88] Moreover, if depolarization was responsible for such an effect, we would expect 3D FE materials to show a more pronounced change in optical constants than 2D FE, as van der Waals FEs are more robust against depolarization.[6] Therefore, it is unlikely that depolarization fields explain the magnitude or the onset of the optical anomaly in CIPS, motivating us to explore alternative intrinsic mechanisms.

Our work points towards a more compelling explanation, involving the interplay between light and ferroelectric polarization. We suggest that the anomalous light-matter interaction may be influenced, or even mediated, by itinerant ionic charge carriers within the crystal structure, an effect largely enhanced in the case of CIPS, compared to $LiNbO_3$ and Bi_2FeCrO_6, due to its distinct crystal structure. Ionic mobility is widely known within CIPS,[23,42,51,89] $LiNbO_3$[90] and Bi_2FeCrO_6.[91] The ionic conductivity activation energy in bulk CIPS is reported to be 1.16 eV perpendicular to the layers and 0.55 eV parallel to the layers in the ferrielectric phase.[51] On the other hand, the activation energy in bulk $LiNbO_3$ and Bi_2FeCrO_6 is reported to be 1.35[92] and 0.77 eV,[91] respectively. The values for these two 3D systems are lower than the activation energy for CIPS, especially for the ionic conduction parallel to the layers, which would explain the differences in the magnitude of the change in refractive index with thickness observed in Figure 5a.

Furthermore, such anomalous interplay would be especially significant in CIPS, known to be a ferro-ionic material, where both ferroelectric polarization and ionic conduction are intrinsically coupled through the Cu(I) spatial instability.[23,42–44] Due to the strong electrostatic interaction between ferroelectric and ionic defect dipoles in CIPS, its polarization switching kinetics is known to be ionic-conduction-limited,[93] and when driven by an in-plane electric field, the movement of Cu(I) cations can induce out-of-plane polarization switching.[43] Moreover, in sister compound $CuCrP_2S_6$, it was recently shown that Cu(I) cation motion (via external field) can tune the refractive index.[94] Thus, a change in the ion mobility of CIPS while decreasing thickness, through a change in the Cu(I) occupancy, could lead to a change in the Cu(I) FE polarization contribution, resulting in a change in optical constants.

It has been reported that the Cu(I) population in CIPS, hence the ion mobility, differs between the monoclinic *Cc* and trigonal $P3_1c$ phases.[47] Consequently, below $t_c \in [60, 71]$ nm, the change in ion mobility with thickness may be caused by its structural transition. At $t \in (71, 170)$ nm, the cause of a change in ion mobility with thickness remains elusive. In Figure S12c, we computed the out-of-plane refractive index wavelength dependence of CIPS via DFT-based calculations (see Subsection 5) for two extreme situations, a full occupancy of Cu(I) cations of the octahedral site within the sulfur framework (Cu^{2u}), and a full occupancy of Cu(I) cations of the quasi-tetrahedral site within the van der Waals gap (Cu^{3u}), as illustrated in Figure S12a. If we qualitatively compare the DFT-based results with the experimental results, and despite the bandgap underestimation of the DFT-based calculations (Figure S12b), we observe a relative agreement between the optical behavior within the thick regime ($t \geqslant 170$ nm)and the behavior for full occupancy of the Cu^{3u} position. Analogously, both the refractive index for the full occupancy of the Cu^{2u} location and the refractive index curves for $t \in (71, 170)$ nm agree reasonably well. The DFT-based calculations show a reduction in magnitude of the out-of-plane refractive index as the Cu(I) localizes out of the van der Waals gap, increasing the occupancy of the Cu^{2u} location, in line with the results reported in ref. [47], supporting our proposition of a change of Cu(I) occupation and, consequently, a change in ionic mobility, while decreasing the thickness of CIPS. Yet, more investigation, both experimental and computational, is still needed to fully understand the mechanism behind the anomalous refractive index modulation in CIPS, but the potential that CIPS holds for electro-optical and photonic applications is now unequivocal.

4. Conclusion

We investigated the optical properties of the 2D ferrielectric $CuInP_2S_6$ over a wide range of thicknesses and wavelengths, and discovered a giant birefringence, maximized at $|\Delta n| \sim 1.24$ at $t \sim 22$ nm and $\lambda = 339.5$ nm, and the presence of an anomalous change in the refractive index of CIPS with thickness in the range $t \in [22, 170)$ nm, as large as $\delta n \sim 23.2\%$. To the best of our knowledge, this is the largest intrinsic birefringence $|n_{OOP} - n_{IP}|$ in the blue-ultraviolet regime of any known material, and the anomalous refractive index behavior reveals a new parameter to control optical response over a wide range of wavelengths and thicknesses, making CIPS an attractive system for electro-optic applications. This effect is shown to be the largest in CIPS, where both its polarization and ionic conductivity are intrinsically coupled; we ascribe changes in the optical response with thickness to changes in the Cu(I) polarization component. However, a complete explanation of the entire anomalous thickness regime is yet to be determined. Backed by DFT-based calculations, we propose a complex and strong thickness-dependent interplay between polarization, light and ion mobility as an explanation for the anomalous nature of CIPS with thickness that we show may be extendable to other ferroelectrics, like $LiNbO_3$, or multiferroics, like Bi_2FeCrO_6, though to a lesser extent compared to CIPS. Further investigation is needed to elucidate such complex interactions, yet our work paves the way for a paradigm shift in electro-optics and photonics based on the CIPS family of materials.

5. Experimental Methods

Sample preparation: The CIPS flake used in this work was mechanically exfoliated directly from a bulk CIPS single crystal (HQ graphene) onto a Si substrate with a thermally grown SiO_2 layer ≈300 nm thick (see Figure 1e top left microscope image). After exfoliation, spectroscopic ellipsometry and Raman spectroscopy measurements were performed.

Spectroscopic ellipsometry—Measurement: The optical constants and thicknesses of the CIPS sample were measured at room temperature using a Woollam M2000XI-210 Variable Angle Spectroscopic Ellipsometer with a spectral range between 210.6 and 1688.3 nm (see Figure 1b). Before starting each of the actual measurements, a mapping scan of the whole flake was performed with a step size of 4.67 µm to select the cleanest and least noisy regions of the CIPS flake plateau. The actual measurements were performed at three different angles of incidence: 65, 70 and 75 degrees. Focus probes were used to reduce the beam spot size to ≈300 µm at 70 degrees. During the measurement, due to the presence of a rotating compensator before the sample and a rotating polarizer and analyzer in the ellipsometer, all elements of the Mueller matrix with the exception of the bottom row (M41 to M44) were measured.

Spectroscopic ellipsometry—Modelling: The ellipsometry data was analysied using the CompleteEase software. An example of the raw ellipsometric spectrum and the corresponding fitting is shown in Figure S1a. The main model is split up into two submodels, a bulk and a thin regime model, and uses a Bruggeman effective medium approximation (EMA) between them. Both the bulk and thin regime models were established using a multi-sample analysis, which enabled simultaneous fitting of different measurements. In this way, the quality of the model increases, as it needs to fit more varied data. Both models start off with a Cauchy-Urbach model to explain the dispersive regions of the spectrum. The Cauchy-Urbach is subsequently fed into a basis spline function with a node distance of 0.5 eV. To make this raw mathematical model physical, a combination of a Cody–Lorentz oscillator and a Gaussian oscillator was built. The same process was followed for the in-plane and out-of-plane axes. Finally, the thin and bulk models were combined with the Bruggeman EMA model. Note that both Maxwell-Garnet and Bruggeman approaches yielded nearly identical outcomes between thickness and refractive index. Considering the properties of CIPS, the most appropriate choice was chosen to be the Bruggeman approximation.

Besides the main model, certain imperfections were also taken into account. A roughness model (consisting of a Bruggeman EMA of 50% air and 50% the current model), a thickness non-uniformity depolarization fit and bandwidth error of the two spectrum analyzers (using a Gaussian overlap function between the 5 nm bandwidth visible-UV and 10 nm bandwidth IR spectrum analyzers) were used.

Other models were also tested as a part of the investigation. However, the most obvious other options (such as graded models) did not yield better fitting results. Therefore, it implies that, in fact, the optical

properties of CIPS actually change with thickness. It should also be noted that the mean square error between fit and model (MSE) was best minimized using anisotropic models and showed improvement in MSE in all cases tested, as expected with van der Waals materials.[77]

Lastly, it has been reported that CIPS also exhibits a small but non-negligible in-plane optical anisotropy $\Delta n = n_x - n_y = 0.0149$.[61] Nevertheless, including trirefringence instead of birefringence did not considerably improve the model, as it is less sensitive to in-plane birefringence. Thus, in-plane optical anisotropy was not considered in this work.

Raman spectroscopy—Measurement: For the bulk flake and the last 20 etches ($t \in [22, 202]$ nm), Raman spectroscopy measurements were included in the measurement cycle, as shown in Figure 1c. A Renishaw Invia Reflex Raman microscope was used at room temperature. Before every measurement, a Si reference substrate was measured to calibrate the instrument. Each spectrum was obtained with an excitation wavelength of 488 nm, a grating of 3000 lines per mm, a power of 0.50 mW, 10 accumulations, 10 s acquisition time, and a 50x objective. The spot size of the Raman microscope used is 1.5 µm. For each thickness, a Raman line scan with a step size of 1 µm was performed across the same homogeneous region of the CIPS flake, obtaining ⩾10 Raman spectra respectively.

Raman spectroscopy—Data analysis: The ⩾10 spectra were averaged and normalized to the ≈375 cm^{-1} peak (most intense peak). Peaks were found using OriginPRO 2024 Find Peaks tool. First, we set a user defined baseline using 8 anchor points. Then, the baseline was fitted using a linear function (an exponential decay fitted baseline was also tried but results did not change significantly). Finally, peaks were found via local maximum method, using 2–4 local points and a peak filtering by height from 2 to 10%, depending on the noisiness of the data.

Argon beam etching: Once the CIPS flake was characterized via ellipsometric and Raman spectroscopies, the sample was dry-etched under a 4 degree sheering angle and a 10 rpm stage rotation with a SCIA Mill150 argon beam etcher, using a beam voltage of 200 V and an acceleration beam voltage of 100 V, as illustrated in Figure 1d. In this etcher, the accelerated Ar ions are neutralized before hitting the sample using electrons produced by a filament under vacuum, with a filament current of 250 mA. All the parameters of the argon beam etcher were not changed during the entirety of this work, independently of the material etched (CIPS, $LiNbO_3$ and SiO_2) except for the etching time, obtaining a constant etch rate, as shown in Figure S1b for the the etching of CIPS.

Atomic Force Microscopy: The topography of the CIPS flake used in this work was measured at room temperature and in a controlled environment inside a glovebox with O_2 and H_2O concentrations below 0.5 ppm using a FlexAFM (Nanosurf). The measurement was performed in tapping mode using a HQ:NSC15/Al BS (MikroMasch) tip.

Atomic Force Microscopy—Piezoresponse force microscopy: The ferroelectric properties of both CIPS and hBN were studied in contact mode using a 12Pt300B (Rocky Mountain Nanotechnology) tip. The measurements for the CIPS flakes were performed in single-frequency mode, with a frequency of 14 kHz (off-resonance) and 6 kHz bandwidth, with an excitation amplitude of 500 mV, 0 V tip voltage, and 300 mV setpoint. The measurements for the hBN flakes were also performed in single-frequency mode, but with a frequency of 10 kHz (off-resonance) and 6 kHz bandwidth, with an excitation amplitude of 1000 mV, 0 V tip voltage, and 50 mV setpoint. Both the CIPS and hBN flakes were previously exfoliated onto a 50 nm Au| 300 nm SiO_2| Si substrate.

Energy dispersive X-ray spectroscopy: The elemental analysis characterization of CIPS before and after argon beam etching was performed in a Nova NanoSEM 450 (FEI) equipped with an EDAX Ametek detector, with an acceleration voltage of 10 kV and an angle of 30°. The flakes were previously exfoliated onto a 50 nm Cr| 300 nm SiO_2| Si substrate.

DFT-based calculations of the refractive index: The refractive index $n(\lambda)$ was obtained from the random phase approximation (RPA) dielectric function as implemented in the Vienna Ab initio Simulation Package (VASP).[95–97] We employed the projector augmented-wave (PAW) basis[98] together with the Perdew–Burke–Ernzerhof (PBE) exchange–correlation functional.[99] Calculations were performed for the experimental crystal structure of $CuInP_2S_6$ (CIPS) in its minimal bulk unit cell containing 20 atoms. To model different local environments, the Cu position was adjusted manually while keeping the lattice constants fixed at a = 6.09560, b = 10.56450, c = 13.62300, α = 90.0000, β = 107.1010, and γ = 90.0000. Two configurations were considered, corresponding to the Cu atom being displaced either further inside or further outside the van der Waals gap. The Brillouin zone was sampled using 5 × 5 × 6 k- and q-point meshes, with a total of 128 bands included in the calculation. Gaussian smearing of 50 meV was applied. The retarded dielectric function was evaluated on a frequency grid ranging from 0 to 10 eV in steps of 0.1 eV, using a complex broadening parameter of 50 meV. The RPA formalism in VASP was employed as described in ref. [100].

Supporting Information

Supporting Information is available from the Wiley Online Library or from the author.

Acknowledgements

The authors acknowledge Heng Wu, Yaojia Wang, Michiel Dubbelman and Victor Vreede for their valuable discussions. The authors also thank Lodi Schriek (spectroscopic ellipsometry and Raman spectroscopy) and Charles de Boer (argon beam etcher) for their experimental support. The authors thank Yanyu Liu and Jiawang Hong for providing the trigonal $P3_1c$ CIF file of CIPS for the preparation of Figure 1a bottom panel. The authors acknowledge the support from the Dutch Research Council (NWO) under the 2023 VIDI Award VI.Vidi.223.089, as well as the Kavli Foundation under the Kavli Institute Innovation Award (KIIA) (LS-2023-GR-14-2778).

Conflict of Interest

The authors declare no conflict of interest.

Author Contributions

H.M.H. and R. J. H.K., contributed equally to this work. H.M.H. conceived the study. H.M.H. and R.J.H.K. designed the study. R. J.H.K. conceived the low-angle argon beam etching. H.M.H. performed the argon beam etching, the spectroscopic ellipsometry, and the Raman spectroscopy measurements. R.J.H.K. created the spectroscopic ellipsometry model. H.M.H performed the AFM and PFM measurements. R. J.H.K. and H.M.H. carried out the EDS measurements. H.M.H. performed the data analysis. T.M.K. prepared the CIF files for the DFT-based calculations. M.R. and S.G. performed the DFT-based calculations. H.M.H. wrote the majority of the manuscript. T.M.K, R.J.H.K., and M.N.A. reviewed the manuscript. M.N.A. is the principal investigator. All authors contributed to the preparation of the manuscript.

Data Availability Statement

The data that support the findings of this study are available from the corresponding author upon reasonable request.

Keywords

birefringence, CIPS, $CuInP_2S_6$, 2D materials, ferroelectrics, ferroionics, optical properties, refractive index; thickness-dependence

Received: July 16, 2025
Revised: September 30, 2025
Published online: November 17, 2025

[1] G. Sinatkas, T. Christopoulos, O. Tsilipakos, E. E. Kriezis, *J. Appl. Phys.* **2021**, *130*, 010901.
[2] E. L. Wooten, K. M. Kissa, A. Yi-Yan, E. J. Murphy, D. A. Lafaw, P. F. Hallemeier, D. Maack, D. V. Attanasio, D. J. Fritz, G. J. McBrien, D. E. Bossi, *IEEE J. Sel. Top. Quantum Electron.* **2000**, *6*, 69.
[3] Y. Hu, D. Zhu, S. Lu, X. Zhu, Y. Song, D. Renaud, D. Assumpcao, R. Cheng, C. J. Xin, M. Yeh, H. Warner, X. Guo, A. Shams-Ansari, D. Barton, N. Sinclair, M. Loncar, *Nat. Rev. Phys.* **2025**, *7*, 237.
[4] J. M. Arrazola, V. Bergholm, K. Brádler, T. R. Bromley, M. J. Collins, I. Dhand, A. Fumagalli, T. Gerrits, A. Goussev, L. G. Helt, J. Hundal, T. Isacsson, R. B. Israel, J. Izaac, S. Jahangiri, R. Janik, N. Killoran, S. P. Kumar, J. Lavoie, A. E. Lita, D. H. Mahler, M. Menotti, B. Morrison, S. W. Nam, L. Neuhaus, H. Y. Qi, N. Quesada, A. Repingon, K. K. Sabapathy, M. Schuld, *Nature* **2021**, *591*, 54.
[5] C. Wang, L. You, D. Cobden, J. Wang, *Nat. Mater.* **2023**, *22*, 542.
[6] D. Zhang, P. Schoenherr, P. Sharma, J. Seidel, *Nat. Rev. Mater.* **2023**, *8*, 25.
[7] A. Mushtaq, L. Clink, M. Y. Noor, C. Kuz, E. Deangelis, R. Siebenaller, A. Fisher, D. Verma, R. C. Myers, B. S. Conner, M. A. Susner, E. Chowdhury, *J. Phys. Chem. Lett.* **2022**, *13*, 10513.
[8] N. Savage, *Nat. Photonics* **2009**, *3*, 170.
[9] M. F. Weber, C. A. Stover, L. R. Gilbert, T. J. Nevitt, A. J. Ouderkirk, *Science* **2000**, *287*, 2451.
[10] X. Chen, B. Zhang, F. Zhang, Y. Wang, M. Zhang, Z. Yang, K. R. Poeppelmeier, S. Pan, *J. Am. Chem. Soc.* **2018**, *140*, 16311.
[11] Z. Xu, B. M. Sadler, *IEEE Commun. Mag.* **2008**, *46*, 67.
[12] F. Zhang, X. Chen, M. Zhang, W. Jin, S. Han, Z. Yang, S. Pan, *Light: Sci. Appl.* **2022**, *11*, 252.
[13] H. Xu, B. Ding, Y. Xu, Z. Huang, D. Wei, S. Chen, T. Lan, Y. Pan, H.-M. Cheng, B. Liu, *Nat. Nanotechnol.* **2022**, *17*, 1091.
[14] W. M. Sinton, *J. Opt. Soc. Am.* **1961**, *51*, 1309.
[15] G. Ghosh, *Opt. Commun.* **1999**, *163*, 95.
[16] L.-L. Ma, C.-Y. Li, J.-T. Pan, Y.-E. Ji, C. Jiang, R. Zheng, Z.-Y. Wang, Y. Wang, B.-X. Li, Y.-Q. Lu, *Light: Sci. Appl.* **2022**, *11*, 270.
[17] M. A. Kats, P. Genevet, G. Aoust, N. Yu, R. Blanchard, F. Aieta, Z. Gaburro, F. Capasso, *Proc. Natl. Acad. Sci. USA* **2012**, *109*, 12364.
[18] W. Zhang, J. Liu, W.-P. Huang, W. Zhao, *IEEE Photonics J.* **2011**, *3*, 512.
[19] D. Weglowska, P. Kula, J. Herman, *RSC Adv.* **2016**, *6*, 403.
[20] S. Zhou, L. You, H. Zhou, Y. Pu, Z. Gui, J. Wang, *Probab Theory Relat Fields* **2021**, *125*, 259.
[21] C. H. Ho, S. F. Hu, H. W. Chang, *FlatChem* **2021**, *29*.
[22] K. Bu, T. Fu, Z. Du, X. Feng, D. Wang, Z. Li, S. Guo, Z. Sun, H. Luo, G. Liu, Y. Ding, T. Zhai, Q. Li, X. Lü, *Chem. Mater.* **2023**, *35*, 242.
[23] V. Maisonneuve, V. B. Cajipe, A. Simon, R. Von Der Muhll, J. Ravez, *Phys. Rev. B* **1997**, *56*, 10860.
[24] I. P. Studenyak, V. V. Mitrovcij, G. S. Kovacs, M. I. Gurzan, O. A. Mykajlo, Y. M. Vysochanskii, V. B. Cajipe, *Phys. Status Solidi (B) Basic Res.* **2003**, *236*, 678.
[25] F. Liu, L. You, K. L. Seyler, X. Li, P. Yu, J. Lin, X. Wang, J. Zhou, H. Wang, H. He, S. T. Pantelides, W. Zhou, P. Sharma, X. Xu, P. M. Ajayan, J. Wang, Z. Liu, *Nat. Commun.* **2016**, *7*, 12357.
[26] L. Niu, F. Liu, Q. Zeng, X. Zhu, Y. Wang, P. Yu, J. Shi, J. Lin, J. Zhou, Q. Fu, W. Zhou, T. Yu, X. Liu, Z. Liu, *Nano Energy* **2019**, *58*, 596.
[27] H. Zhu, J. Li, Q. Chen, W. Tang, X. Fan, F. Li, L. Li, *ACS Nano* **2023**, *17*, 1239.
[28] X. Jiang, X. Wang, X. Wang, X. Zhang, R. Niu, J. Deng, S. Xu, Y. Lun, Y. Liu, T. Xia, J. Lu, J. Hong, *Nat. Commun.* **2022**, *13*, 574.
[29] L. You, Y. Zhang, S. Zhou, A. Chaturvedi, S. A. Morris, F. Liu, L. Chang, D. Ichinose, H. Funakubo, W. Hu, T. Wu, Z. Liu, S. Dong, J. Wang, *Sci. Adv.* **2019**, *5*, eaav3780.
[30] Y. Li, J. Fu, X. Mao, C. Chen, H. Liu, M. Gong, H. Zeng, *Nat. Commun.* **2021**, *12*, 5896.
[31] W. Ming, B. Huang, S. Zheng, Y. Bai, J. Wang, J. Wang, J. Li, *Sci. Adv.* **2022**, *8*, eabq1232.
[32] F. Xue, C. Zhang, S. Zheng, P. Tong, B. Wang, Y. Peng, Z. Wang, H. Xu, Y. He, H. Zhou, N. Wang, P. Han, Y. Yuan, Y. Ma, C. Huan, S. Zhang, H. Chen, H. Zhu, Y. Xu, B. Yu, J. Sun, H. Wang, P. Chen, X. Gao, K. Chang, H. Tian, J. Wang, X. Zhang, *Nat. Commun.* **2025**, *16*, 2349.
[33] D. Li, X. Hou, F. Kong, K. Wang, X. Hong, *ACS Nano* **2024**.
[34] M. Si, A. K. Saha, P.-Y. Liao, S. Gao, S. M. Neumayer, J. Jian, J. Qin, N. B. Wisinger, H. Wang, P. Maksymovych, W. Wu, S. K. Gupta, P. D. Ye, *ACS Nano* **2019**, *13*, 8760.
[35] W. F. Io, M. C. Wong, S. Y. Pang, Y. Zhao, R. Ding, F. Guo, J. Hao, *Nano Energy* **2022**, *99*, 107371.
[36] P. Li, A. Chaturvedi, H. Zhou, G. Zhang, Q. Li, J. Xue, Z. Zhou, S. Wang, K. Zhou, Y. Weng, F. Zheng, Z. Shi, E. H. T. Teo, L. Fang, L. You, *Adv. Funct. Mater.* **2022**, *32*, 2201359.
[37] Z. Shang, L. Liu, G. Wang, H. Xu, Y. Cui, J. Deng, Z. Lou, Y. Yan, J. Deng, S.-T. Han, T. Zhai, X. Wang, L. Wang, X. Wang, *ACS Nano* **2024**, *18*, 30530.
[38] F. Kong, L. Zhang, T. Cong, Z. Wu, K. Liu, C. Sun, L. Pan, D. Li, *J. Appl. Phys.* **2022**, *132*, 044103.
[39] D. Qiu, P. Hou, J. Wang, X. Ouyang, *Appl. Phys. Lett.* **2023**, *123*, 042105.
[40] X. Jiang, X. Zhang, Z. Deng, J. Deng, X. Wang, X. Wang, W. Yang, *Nat. Commun.* **2024**, *15*, 10822.
[41] V. Samulionis, J. Banys, Y. Vysochanskii, V. Cajipe, in *Ferroelectrics* **2001**, *257*, 113.
[42] V. Maisonneuve, J. M. Reau, M. Dong, V. B. Cajipe, C. Payen, J. Ravez, *Ferroelectrics* **1997**, *196*, 257.
[43] D. D. Xu, R. R. Ma, Y. F. Zhao, Z. Guan, Q. L. Zhong, R. Huang, P. H. Xiang, N. Zhong, C. G. Duan, *J. Mater. Chem. C* **2020**, *8*, 6966.
[44] D. Zhang, Z. D. Luo, Y. Yao, P. Schoenherr, C. Sha, Y. Pan, P. Sharma, M. Alexe, J. Seidel, *Nano Lett.* **2021**, *21*, 995.
[45] J. Deng, Y. Liu, M. Li, S. Xu, Y. Lun, P. Lv, T. Xia, P. Gao, X. Wang, J. Hong, *Small* **2020**, *16*, 1904529.
[46] Y. Hu, H. Gao, Z. Zhou, S. Wang, Q. Li, Z. Luo, R. Feng, Y. Hou, T. Ying, Y. Weng, Y. Han, L. Fang, L. You, *Appl. Phys. Rev.* **2024**, *11*, 041423.
[47] Y. Bai, W. Hao, Y. Wang, J. Tian, C. Wang, Y. Lei, Y. Yang, X. Yao, Q. Liu, C. Li, M. Gu, J. Wang, *PRX Energy* **2024**, *3*, 023004.
[48] C. Song, S. Zhou, X. Wang, X. He, K. Wu, *Phys. Rev. B* **2023**, *107*, 174109.
[49] $CuInP_2S_6$ crystal structure: Datasheet from pauling file in: Inorganic solid phases, springer materials (online database), **2022**, https://materials.springer.com/isp/crystallographic/docs/sd_1011502, (accessed: February, 2025).
[50] R.-R. Ma, D.-D. Xu, Z. Guan, X. Deng, F. Yue, R. Huang, Y. Chen, N. Zhong, P.-H. Xiang, C.-G. Duan, *Appl. Phys. Lett.* **2020**, *117*, 131102.
[51] A. Dziaugys, J. Banys, J. Macutkevic, Y. Vysochanskii, *Phase Transitions* **2013**, *86*, 878.
[52] Y. Vysochanskii, R. Yevych, L. Beley, V. Stephanovich, V. Mytrovcij, O. Mykajlo, A. Molnar, M. Gurzan, *Ferroelectrics* **2003**, *284*, 161.
[53] A. Kohutych, V. Liubachko, V. Hryts, Y. Shiposh, M. Kundria, M. Medulych, K. Glukhov, R. Yevych, Y. Vysochanskii, *Mol. Cryst. Liq. Cryst.* **2022**, *747*, 14.
[54] Y. Wang, E. A. Irene, *Journal of Vacuum Science & Technology B: Microelectronics and Nanometer Structures Processing, Measurement, and Phenomena* **2000**, *18*, 279.
[55] J. N. Hilfiker, M. Stadermann, J. Sun, T. Tiwald, J. S. Hale, P. E. Miller, C. Aracne-Ruddle, *Appl. Surf. Sci.* **2017**, *421*, 508.
[56] Q. Y. Cai, Y. X. Zheng, P. H. Mao, R. J. Zhang, D. X. Zhang, M. H. Liu, L. Y. Chen, *J. Phys. D: Appl. Phys.* **2010**, *43*, 445302.

[57] Z. J. Xu, F. Zhang, R. J. Zhang, X. Yu, D. X. Zhang, Z. Y. Wang, Y. X. Zheng, S. Y. Wang, H. B. Zhao, L. Y. Chen, *Appl. Phys. A: Mater. Sci. Proc.* **2013**, *113*, 557.
[58] D. X. Zhang, Y. X. Zheng, Q. Y. Cai, W. Lin, K. N. Wu, P. H. Mao, R. J. Zhang, H. B. Zhao, L. Y. Chen, *Appl. Phys. A: Mater. Sci. Proc.* **2012**, *108*, 975.
[59] B. A. Ali, A. Bouhmouche, L. Wendling, C. Hu, C. Bouillet, G. Schmerber, A. M. Saeedi, S. Zafeiratos, V. Papaefthimiou, R. Moubah, S. Colis, *Vacuum* **2023**, *216*, 112411.
[60] R. N. Verrone, C. Moisset, F. Lemarchand, A. Campos, M. Cabié, C. Perrin-Pellegrino, J. Lumeau, J. Y. Natoli, K. Iliopoulos, *ACS Appl. Nano Mater.* **2020**, *3*, 7963.
[61] Y. Liu, Y. Wu, R. Duan, J. Fu, M. Ovesen, S. C. E. Lai, T. E. Yeo, J. Y. Chee, Y. Chen, S. L. Teo, H. R. Tan, W. Zhang, J. K. Yang, K. S. Thygesen, Z. Liu, Y. W. Zhang, J. Teng, *Adv. Mater.* **2024**, *36*, 2401838.
[62] A. K. Hamze, M. Reynaud, J. Geler-Kremer, A. A. Demkov, *npj Comput. Mater.* **2020**, *6*, 130.
[63] M. Jazbinšek, M. Zgonik, *Appl. Phys. B: Lasers Opt.* **2002**, *74*, 407.
[64] A. Ross, M. S. M. M. Ali, A. Saha, R. Zu, V. Gopalan, I. Dabo, L.-Q. Chen, *Phys. Rev. B* **2025**, *111*, 8.
[65] G. H. Haertling, *Ferroelectrics* **1987**, *75*, 25.
[66] A. Dey, Ph.D. thesis, University of Nottingham, Nottingham, UK.
[67] R. Selhorst, S. Lough, J. Jiang, B. S. Conner, J. T. Goldstein, A. N. Giordano, E. Rowe, M. Ishigami, R. Pachter, M. A. Susner, R. Rao, *Chem. Mater.* **2024**, 7822.
[68] S. N. Neal, S. Singh, X. Fang, C. Won, F.-t. Huang, S.-W. Cheong, K. M. Rabe, D. Vanderbilt, J. L. Musfeldt, *Phys. Rev. B* **2022**, *105*, 075151.
[69] R. Rao, R. Selhorst, B. S. Conner, M. A. Susner, *Phys. Rev. Mater.* **2022**, *6*, 045001.
[70] M. Deluca, What can i learn about ferroelectrics with raman spectroscopy? presented at the ferrotalks webinar series, **2020**, https://youtu.be/0_7GFymGRxo?list=PL02l257Y5pIAwwmKv_VqjbyOXQ9NigXWp, (accessed: October 2024).
[71] C. Song, J. Huang, H. Huang, G. Zhao, X. He, K. Wu, *Phys. Rev. B* **2024**, *109*, 174109.
[72] R. N. Smartt, W. H. Steel, *J. Opt. Soc. Am.* **1959**, *49*, 710.
[73] D. E. Zelmon, D. L. Small, D. Jundt, *J. Opt. Soc. Am. B* **1997**, *14*, 3319.
[74] B. Zysset, I. Biaggio, P. Günter, *J. Opt. Soc. Am. B* **1992**, *9*, 380.
[75] D. V. Grudinin, G. A. Ermolaev, D. G. Baranov, A. N. Toksumakov, K. V. Voronin, A. S. Slavich, A. A. Vyshnevyy, A. B. Mazitov, I. A. Kruglov, D. A. Ghazaryan, A. V. Arsenin, K. S. Novoselov, V. S. Volkov, *Mater. Horiz.* **2023**, *10*, 2427.
[76] G. A. Ermolaev, D. V. Grudinin, Y. V. Stebunov, K. V. Voronin, V. G. Kravets, J. Duan, A. B. Mazitov, G. I. Tselikov, A. Bylinkin, D. I. Yakubovsky, S. M. Novikov, D. G. Baranov, A. Y. Nikitin, I. A. Kruglov, T. Shegai, P. Alonso-González, A. N. Grigorenko, A. V. Arsenin, K. S. Novoselov, V. S. Volkov, *Nat. Commun.* **2021**, *12*, 854.
[77] B. Munkhbat, P. Wróbel, T. J. Antosiewicz, T. O. Shegai, *ACS Photonics* **2022**, *9*, 2398.
[78] Q. Guo, Q. Zhang, T. Zhang, J. Zhou, S. Xiao, S. Wang, Y. P. Feng, C. W. Qiu, *Nat. Photonics* **2024**, *18*, 1170.
[79] H. Yang, H. Jussila, A. Autere, H.-P. Komsa, G. Ye, X. Chen, T. Hasan, Z. Sun, *ACS Photonics* **2017**, *4*, 3023.
[80] N. Mao, J. Tang, L. Xie, J. Wu, B. Han, J. Lin, S. Deng, W. Ji, H. Xu, K. Liu, L. Tong, J. Zhang, *J. Am. Chem. Soc.* **2016**, *138*, 300.
[81] S. Niu, G. Joe, H. Zhao, Y. Zhou, T. Orvis, H. Huyan, J. Salman, K. Mahalingam, B. Urwin, J. Wu, Y. Liu, T. E. Tiwald, S. B. Cronin, B. M. Howe, M. Mecklenburg, R. Haiges, D. J. Singh, H. Wang, M. A. Kats, J. Ravichandran, *Nat. Photonics* **2018**, *12*, 392.
[82] Y. Li, K. M. Ok, *Angew. Chem., Int. Ed.* **2024**, *63*, e202409336.
[83] Y. Wang, M. Xia, J. Zhou, D. Huang, Y. Chen, X. Zhang, *Laser Photonics Rev.* **2024**, *18*, 2301088.
[84] Y. Wu, L. Wang, H. Li, Q. Dong, S. Liu, *Chin. Chem. Lett.* **2022**, *33*, 153.
[85] L. Chen, Y. Li, C. Li, H. Wang, Z. Han, H. Ma, G. Yuan, L. Lin, Z. Yan, X. Jiang, J. M. Liu, *AIP Adv.* **2019**, *9*.
[86] P. Würfel, I. P. Batra, *Ferroelectrics* **1976**, *12*, 55.
[87] J. Y. Li, *Mech. Mater.* **2009**, *41*, 1125.
[88] P. Gao, Z. Zhang, M. Li, R. Ishikawa, B. Feng, H. J. Liu, Y. L. Huang, N. Shibata, X. Ma, S. Chen, J. Zhang, K. Liu, E. G. Wang, D. Yu, L. Liao, Y. H. Chu, Y. Ikuhara, *Nat. Commun.* **2017**, *8*.
[89] S. Neumayer, H. Qiao, N. Balke, *Appl. Phys. Lett.* **2025**, *126*.
[90] E. Strelcov, A. V. Ievlev, S. Jesse, I. I. Kravchenko, V. Y. Shur, S. V. Kalinin, *Adv. Mater.* **2014**, *26*, 958.
[91] M. Mahapatra, D. K. Pati, B. Sahu, P. K. Sahoo, R. K. Parida, B. N. Parida, R. Padhee, *J. Mater. Sci.: Mater. Electron.* **2024**, *35*, 582.
[92] C. Kofahl, L. Dörrer, B. Muscutt, S. Sanna, S. Hurskyy, U. Yakhnevych, Y. Suhak, H. Fritze, S. Ganschow, H. Schmidt, *Phys. Rev. Mater.* **2023**, *7*, 033403.
[93] S. Zhou, L. You, A. Chaturvedi, S. A. Morris, J. S. Herrin, N. Zhang, A. Abdelsamie, Y. Hu, J. Chen, Y. Zhou, S. Dong, J. Wang, *Mater. Horiz.* **2020**, *7*, 263.
[94] G. Dushaq, S. Serunjogi, S. R. Tamalampudi, M. Rasras, *Light: Sci. Appl.* **2024**, *13*, 92.
[95] G. Kresse, J. Hafner, *Phys. Rev. B* **1993**, *47*, 558.
[96] G. Kresse, J. Furthmüller, *Comput. Mater. Sci.* **1996**, *6*, 15.
[97] G. Kresse, J. Furthmüller, *Phys. Rev. B* **1996**, *54*, 11169.
[98] P. E. Blöchl, *Phys. Rev. B* **1994**, *50*, 17953.
[99] J. P. Perdew, K. Burke, M. Ernzerhof, *Phys. Rev. Lett.* **1996**, *77*, 3865.
[100] M. Gajdoš, K. Hummer, G. Kresse, J. Furthmüller, F. Bechstedt, *Phys. Rev. B* **2006**, *73*, 045112.